

Design Proposal: Mach-Zehnder Interferometer

FELIPE SOUZA SANCHES¹

¹ *edx PhotIx - Username: FelipeSouzaSanches*
**felipess37@gmail.com*

Abstract: This study investigates the performance of single-mode Silicon MZIs (500×220 nm) under fundamental TE polarization. By implementing intentional path length imbalances (ΔL) of 100, 150, and 200 μm , we demonstrate a methodical approach to extracting waveguide properties. The following sections outline the MZI theory, the simulation parameters, and a detailed verification of these models through experimental analysis.

1. Introduction

Modern optical communication relies heavily on silicon photonics, a field that benefits from the mature infrastructure of CMOS foundries to achieve high-volume production [1]. This technology enables the integration of intricate optical systems onto single, compact chips [2]. At the heart of many such systems is the Mach-Zehnder Interferometer (MZI), an indispensable component used for everything from signal modulation to wavelength filtering [3].

The current work details the design of several MZI configurations specifically intended to measure waveguide group indices through experimental means. These designs are optimized for E-beam lithography to guarantee reliable fabrication. We provide a comprehensive overview of the underlying theory, component-level modeling, and the specific design iterations used in this study.

2. Theory

As shown in Fig. 1, an MZI functions by splitting light into two waveguides and then bringing them back into a single output. By introducing a specific path imbalance, we can trigger interference during the recombination process. This makes the device's transmission highly sensitive to the wavelength, resulting in the characteristic fringe pattern seen in the results.

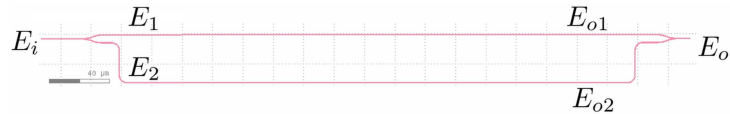


Fig. 1. Conceptual setup of our unbalanced interferometer. By splitting E_i into two arms (L_1 and L_2) and then recombining them, we create a path-length-dependent output E_o that allows us to characterize the waveguide's behavior.

3. Theoretical Framework

The operational principle of the Mach-Zehnder Interferometer (MZI) relies on the interference between two light paths. As illustrated in Fig. 1, an initial Y-junction serves as a 3-dB splitter, distributing the input electric field E_i equally into the upper and lower arms. As these fields propagate along their respective paths of length L_1 and L_2 , they accumulate phase and undergo attenuation. The electric fields immediately preceding the recombination junction, E_{o1} and E_{o2} , are expressed as:

$$E_{o1} = \frac{E_i}{\sqrt{2}} \exp\left(-i\beta_1 L_1 - \frac{\alpha_1}{2} L_1\right) \quad (1)$$

$$E_{o2} = \frac{E_i}{\sqrt{2}} \exp\left(-i\beta_2 L_2 - \frac{\alpha_2}{2} L_2\right) \quad (2)$$

In these expressions, α_1 and α_2 represent the power attenuation coefficients, while the propagation constants $\beta_{1,2}$ are determined by the effective refractive index $n_{1,2}$ of the guided modes:

$$\beta = \frac{2\pi n_{eff}}{\lambda} \quad (3)$$

At the second Y-junction, the fields undergo coherent recombination, resulting in the total output field E_o :

$$E_o = \frac{1}{\sqrt{2}}(E_{o1} + E_{o2}) = \frac{E_i}{2} \left[\exp\left(-i\beta_1 L_1 - \frac{\alpha_1}{2} L_1\right) + \exp\left(-i\beta_2 L_2 - \frac{\alpha_2}{2} L_2\right) \right] \quad (4)$$

Since the optical intensity I is proportional to the square of the electric field magnitude ($I \propto |E|^2$), the general expression for the output intensity I_o is given by:

$$I_o = \frac{I_i}{4} \left| \exp\left(-i\beta_1 L_1 - \frac{\alpha_1}{2} L_1\right) + \exp\left(-i\beta_2 L_2 - \frac{\alpha_2}{2} L_2\right) \right|^2 \quad (5)$$

For the purpose of this analysis, we can simplify this expression by assuming nearly lossless waveguides ($\alpha_1 = \alpha_2 \approx 0$). Furthermore, given that the waveguides in both arms are structurally identical, they share the same effective index ($n_1 = n_2 = n_{eff}$) and propagation constant ($\beta_1 = \beta_2 = \beta$). Under these conditions, the interference becomes solely a function of the physical path length difference, $\Delta L = L_2 - L_1$:

$$I_o = \frac{I_i}{2} [1 + \cos(\beta \Delta L)] \quad (6)$$

This relationship is often more conveniently expressed via the normalized transfer function:

$$\frac{I_{out}}{I_{in}} = \cos^2\left(\frac{\Delta\phi}{2}\right) \quad (7)$$

where the total phase difference $\Delta\phi$ is defined as:

$$\Delta\phi = \beta \Delta L = \frac{2\pi n_{eff}}{\lambda} \Delta L \quad (8)$$

The periodic nature of Eq. 7 results in a transmission spectrum characterized by distinct interference fringes. These spectral peaks and nulls provide the experimental basis for extracting the waveguide's group index.

3.1. Free Spectral Range (FSR) and Group Index Extraction

A key metric for characterizing the device's spectral response is the **Free Spectral Range (FSR)**, defined as the wavelength interval between two successive transmission maxima. Physically, this corresponds to the span over which the relative phase difference between the arms shifts by 2π . For an imbalanced MZI, the FSR is a function of both the physical path imbalance (ΔL) and the waveguide group index (n_g), expressed by the standard relation [3]:

$$FSR = \frac{\lambda^2}{n_g \Delta L} \quad (9)$$

4. Modelling and Simulation

4.1. Waveguide Design and Modal Analysis

The devices utilize a standard **strip waveguide** architecture, chosen specifically for its fabrication robustness and reliable performance. Given the fixed **220 nm** silicon thickness provided by our foundry process, we settled on a waveguide width of **500 nm**. This geometry is a standard industry benchmark for the C-band, as it maintains high modal confinement while strictly supporting single-mode operation for the fundamental **quasi-TE polarization**, as presented in Fig. 2. Such a configuration is advantageous for suppressing higher-order mode interference and maintaining low propagation losses [4].

To accurately characterize the modal properties of the chosen geometry, we performed numerical simulations of the waveguide cross-section using a commercial-grade eigenmode solver [5]. This allowed for the precise extraction of the effective index and dispersion characteristics necessary for the MZI design.

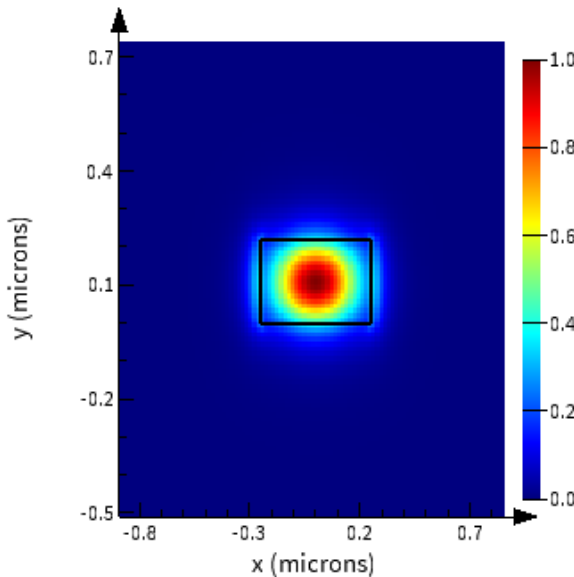


Fig. 2. Simulated E-field intensity for the fundamental TE mode, highlighting the high degree of optical confinement achieved within the silicon core. This localized field distribution confirms that the majority of the optical power is shielded from the cladding, which is essential for reducing parasitic losses.

4.2. Circuit Simulation Setup

The complete circuit response was modeled using the Lumerical INTERCONNECT circuit simulator, with the layout configuration depicted in Fig. 3. This system-level simulation integrates the dispersive waveguide properties calculated in the previous section with pre-characterized S-parameter models for the grating couplers and Y-branches. By combining these physics-based components, we can accurately predict the spectral behavior of the fabricated device.

The spectral response of the input and output grating couplers is illustrated in Fig. 4. The data reveals a characteristic Gaussian-like profile with peak transmission centered near 1550 nm, confirming that the couplers are well-aligned with the target C-band wavelength range.

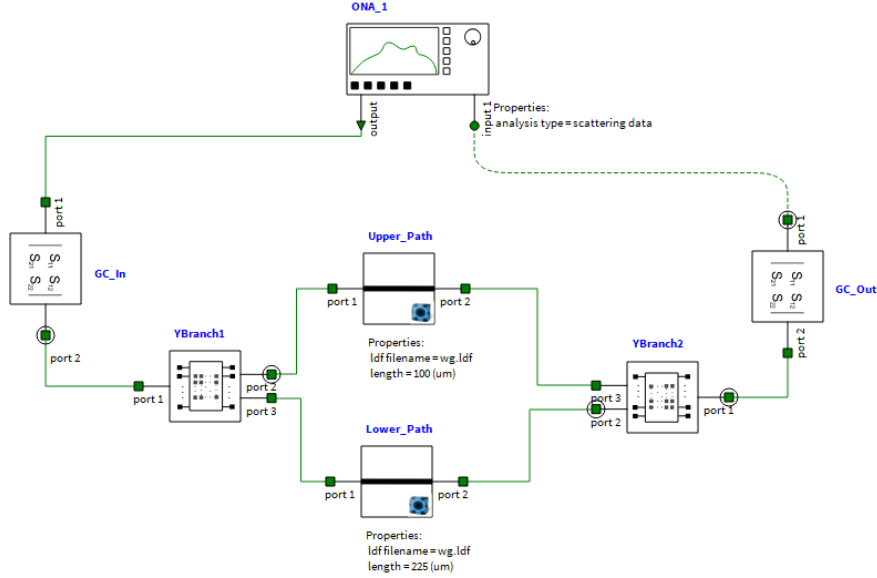


Fig. 3. System-level circuit architecture within the Lumerical INTERCONNECT environment. The schematic illustrates the integrated simulation workflow, where the analytically defined waveguide segments are interfaced with the measured S-parameters of the Y-junctions and grating couplers to capture the full spectral response of the MZI.

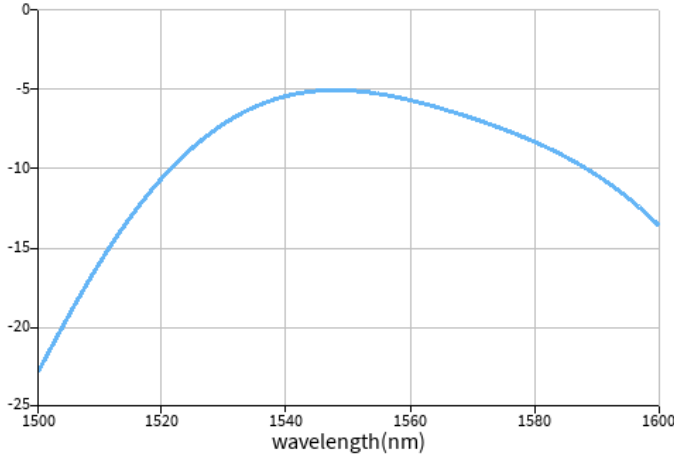


Fig. 4. Simulated transmission characteristics for a back-to-back grating coupler configuration. The spectrum exhibits the expected envelope response, with the transmission maximum aligned to the 1550 nm design target to ensure optimal power throughput for the MZI measurements.

The simulated spectral response for the Y-branch splitter is presented in Fig. 5. The device exhibits a stable, broadband insertion loss of approximately 3 dB across the C-band, verifying that the input power is partitioned equally with minimal parasitic loss. This consistent performance is

vital for maintaining high extinction ratios in the final MZI transmission.

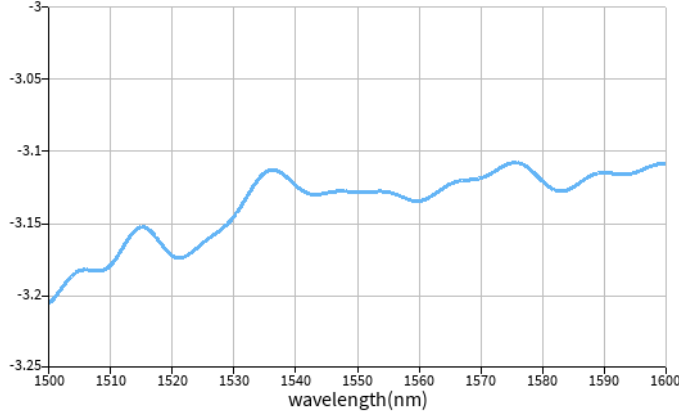


Fig. 5. Simulated transmission spectrum of the Y-branch splitter, demonstrating broadband 3-dB power splitting.

4.3. MZI Design Variations

To empirically determine the group index and validate our theoretical models, we implemented three MZI configurations with varying path length imbalances. By maintaining a constant waveguide cross-section and using identical Y-junctions across all designs, we ensured that any observed spectral changes were exclusively a function of the path difference, ΔL .

Table 1 summarizes the geometric parameters for each design along with the analytically predicted FSR, calculated at a center wavelength of 1550 nm using the simulated group index ($n_g \approx 4.197$).

Table 1. MZI Design Parameters and Predicted Free Spectral Range

Design #	Width	Mode	L_1 (μm)	L_2 (μm)	ΔL (μm)	Expected FSR (nm)
1	500 nm	TE	50	100	50	11.45
2	500 nm	TE	50	150	100	5.72
3	500 nm	TE	50	200	150	3.82

The physical implementation of these designs was captured in a GDSII mask layout using KLayout, as shown in Fig. 6a. Following the layout phase, we extracted the circuit parameters to perform frequency-domain simulations. The resulting transmission spectra for the three imbalance cases, $\Delta L = 50$ μm, 100 μm, and 150 μm, are presented in Figs. 6b, 6c, and 6d, respectively. These results confirm the expected inverse relationship between the path imbalance and the fringe periodicity.

5. Fabrication

To be completed later.

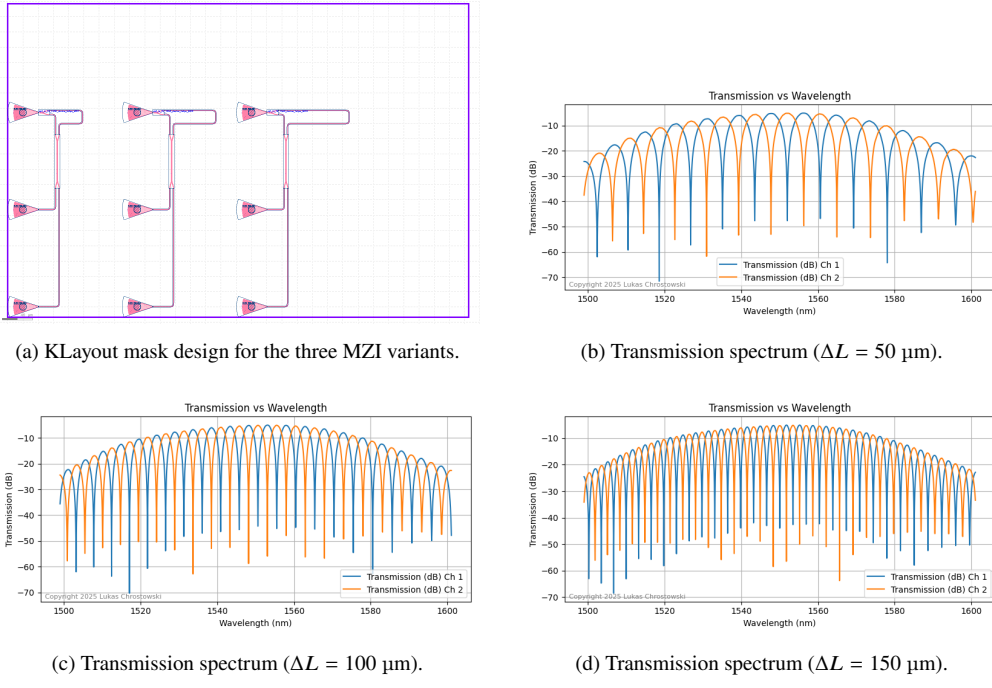


Fig. 6. MZI design and simulated spectral responses: (a) mask layout, and (b–d) transmission spectra illustrating the dependence of FSR on path length imbalance.

6. Experiment data

To be completed later.

7. Analysis

To be completed later.

8. Conclusion

To be completed later.

References

1. R. A. Soref, “Silicon-based optoelectronics,” Proc. IEEE **81**, 1687–1706 (1993).
2. T. Baehr-Jones and M. Hochberg, “The race to commercialize silicon photonics,” IEEE Spectr. **49**, 38–60 (2012).
3. L. Chrostowski and M. Hochberg, *Silicon Photonics Design: From Devices to Systems* (Cambridge University Press, 2015).
4. B. Jalali and S. Fathpour, “Silicon photonics,” J. Light. Technol. **24**, 992–1013 (2006).
5. Ansys Lumerical, “Photonics simulation software,” <https://www.ansys.com/products/photonics> (2024). Accessed: September 23, 2024.